A BIO-INSPIRED, ASYNCHRONOUS, TIME-DOMAIN, MULTISPECTRAL IMAGING SYSTEM FOR HIGH DYNAMIC RANGE NEAR-INFRARED FLUORESCENCE IMAGE-GUIDED SURGERY

BY

STEVEN MICHAEL BLAIR

THESIS

Submitted in partial fulfillment of the requirements
for the degree of Master of Science in Electrical and Computer Engineering
in the Graduate College of the
University of Illinois at Urbana-Champaign, 2018

Urbana, Illinois

Adviser:

Associate Professor Viktor Gruev

ABSTRACT

As surgery has become the standard-of-care for cancer, surgeons have been left underequipped to identify tumors in the operating room, causing many operations to end in positive margins and necessitating secondary treatments to remove remaining tumor tissue. Near-infrared fluorescence image-guided surgery utilizes near-infrared fluorescent markers and near-infrared sensitive cameras to highlight cancerous tissues. Unfortunately, state-of-the-art imaging systems are unable to handle the high dynamic range between strong surgical lighting and weak fluorescent emission and suffer from temperature-dependent co-registration error. To provide a cost-effective and space-efficient imaging system with sufficient dynamic range and no co-registration error, this work analyzes the required dynamic range for a single-sensor imaging system used for near-infrared fluorescence image-guided surgery and reports the development of a single-chip snapshot multispectral imaging system that meets this specification. By monolithically integrating an asynchronous time-domain image sensor and pixelated interference filters, this system achieves a dynamic range of 120 dB without co-registration error in four channels across the visible and near-infrared spectra. The imager can detect less than 100 nM of the FDA-approved fluorescent dye indocyanine green under surgical lighting conditions, making it a promising candidate for image-guided surgery clinical trials.

COPYRIGHT NOTICE

FUNDING NOTICE

To Mom and Dad: For always believing in me.

ACKNOWLEDGMENTS

So many people have worked to enable this research that it would be difficult to list everyone; however, I want to take this opportunity to thank a few key people. First, I would like to thank my adviser, Dr. Viktor Gruev, for his guidance and encouragement as I have stepped into the world of biomedical imaging and started my career in academic research. Over the past two and a half years, he has exemplified the traits that are demanded to make an impact through research—from the vision required to recognize the problems that matter to the skills needed to develop the solutions that stand the test of time. In project after project, he has challenged me to think critically about what I am doing and why I am doing it and has pushed me to tackle taller obstacles and search for deeper truths—leaving me with nothing but excitement for what is left to come.

Second, I would like to thank my labmates, Nan Cui and Missael Garcia, for their help and support as I have entered the research group and joined the academic family. Their patience when I have joined their experiments and their guidance as I have started my own have left a permanent mark on my scientific style, and our conversations on everything from the minutiae of laboratory technique to the big picture of academic research have provided constant inspiration as I have searched for the answers of today and the problems of tomorrow.

Last, but certainly not least, I would like to thank my mom and dad, Karla and Michael Blair, for the love and support that they have provided throughout all these years. For as long as I can remember, I have been allowed to explore my interests, have been pushed to do my best, and have been provided everything that I needed to succeed. Although I am only at the start of my career, I will be forever grateful for the work that they have done and the sacrifices that they have made so that I can be here today, working to understand the world and trying to improve the lives of everyone in it.

TABLE OF CONTENTS

CHAPTER 1   INTRODUCTION

1.1 The Problem in the Operating Room

While surgery has become the primary curative option for patients suffering from many types of cancer, surgeons are often ill-equipped to identify tumors during surgical resection. Despite major advances in preoperative and postoperative imaging modalities that make it possible to identify the location and shape of tumors with unprecedented precision, most surgeons are equipped only with the senses of sight and touch when differentiating healthy tissues from diseased tissue in the operating room. Unfortunately, the low visual contrast between the tumor edge and the surrounding healthy tissue means that incomplete resection is very common. Studies have shown that 21% of patients with oral cancer [2], 4%-40% of patients with prostate cancer [3], and 20%-70% of patients with breast cancer who undergo surgery will have positive tumor margins, necessitating secondary surgeries and radiation treatments [4], [5]. Unfortunately, secondary surgeries are expensive and have limited success rates due to the difficulty of identifying diffuse microscopic cells through scar tissue, and radiation treatment is further associated with adverse effects.

To provide surgeons with the critical information needed to make treatment-time decisions, an intraoperative imaging modality for identifying tumors and other anatomic features is needed. By combining near-infrared fluorescent (NIRF) molecular markers with near-infrared (NIR)

sensitive cameras, NIRF image-guided surgery (IGS) has arisen as a compelling option. Taking advantage of the low absorption coefficient of water and hemoglobin as well as the low auto-fluorescence of tissue in the NIR spectrum, NIRF IGS enables the visualization of both untargeted and targeted probes at several millimeters depth in tissue with low background noise. The US Food and Drug Administration (FDA) has approved two NIRF dyes, indocyanine green (ICG) and methylene blue (MB), which are non-specific molecular markers commonly used to map sentinel lymph nodes and to assess blood perfusion [6]–[8], and many researchers are working to develop tumor-targeted molecular probes with several projects moving into advanced clinical trials.

In response to the proliferation of NIRF IGS molecular markers, several research and industry groups have developed multispectral imaging systems for fluorophore detection, and the FDA has approved a variety of these camera systems for NIRF IGS applications [8]–[10]. Due to the cost and the bulk of these instruments, adoption has been limited to large clinical centers, but in addition to these logistical issues, two major technical issues have been observed. First, the specifications describing surgical light sources and the physics underlying NIRF markers generate a high dynamic range generally exceeding 100 dB between the very bright surgical lighting in the visible spectrum and the very dim fluorescent emission in the NIR spectrum [8], [11]. An imaging system with a lower dynamic range risks producing sub-optimal images or requires changes to the surgical protocol that can disrupt the surgical workflow. Second, the conventional optical architecture of the imaging systems requires a tree of beam splitters and image sensors to isolate spectral channels, yielding a complex optical train that is susceptible to co-registration error as optics expand and contract with temperature gradients [8], [12]. This temperature-dependent co-registration error can result in improper resection of the tumor or iatrogenic damage to surrounding tissue. For proper integration into the operating room, then, these existing camera systems must

2

not only become smaller and simpler but must also be developed with the high dynamic range and low co-registration error demanded by NIRF IGS.

1.2 A Solution from Natural Vision

In the search for high performance image sensors for demanding applications, engineers have sought inspiration from many sources, but none has proven as deep or as rich as nature. Thanks to the wide range of contexts and threats that exist in the wild, natural selection has given rise to visual systems with diverse architectures and unique properties. For instance, animals have found countless ways to utilize spectral information, from the 4-channel vision of birds that enables detailed discrimination between plumage colors to the 12-channel vision of the mantis shrimp that facilitates rapid-fire color recognition—in both cases, their eyes have specifically developed to the task with extra cone cells and special photosensitive structures [13], [14]. Nonetheless, certain features like the ability to record scenes with high dynamic range and to adjust to changes in illumination have been prized across nearly all visual systems. A variety of mechanisms for modifying the sensitivity of photoreceptors have been proposed [15], but theories and experiments alike support both the local alteration of photosensitive structures in the eye and the temporal modulation of neural signals sent from the eye to the brain. Furthermore, it is necessary that visual information be spatiotemporally co-registered in all animals to permit decision-making, a task that is facilitated using compact and regular sensory architectures that permit data fusion using quick and simple neural pathways.

As an example of these concepts, it is worthwhile to consider the compound eye of the morpho butterfly. Each of the eye-like units called ommatidia that compose the compound eye consists of a corneal lens and crystalline cone that collect and focus light, a tract of pigmented cells and nerve fibers that absorb colored light and transmit neural signals, and a stack of air and

3

cytoplasm known as a tapetal filter that serves as an optical interference filter that preferentially reflects different wavelengths [16], [17]. As light passes through the ommatidium, a fraction is absorbed by the pigmented cells, and of what remains, another fraction within the spectral band of the tapetal filter reflects off the air-cytoplasm stack and returns through the pigmented cells [18]. The light absorbed by the pigmented cells across the two passes generates a membrane potential on the neural fiber, and when the membrane potential reaches a critical threshold, a spiked signal is sent to the insect's brain. As the light intensity grows larger, the membrane potential develops faster, and the frequency of the spikes increases unless temporally filtered by the feedback loops in the neural system [19]. Consequently, the combination of the interference filter's structure and the pigmented filter's spectral response determines the spectral band of the ommatidium, and the delay between the spikes that are generated by the incident illumination within these spectral bands encodes the light intensity at the ommatidium. With each ommatidium acting continuously and independently, the brain is constantly and asynchronously monitoring the environment's brightness over a large range of light intensities to generate the co-registered and high dynamic range images that guide the butterfly through daily life.

To address the problems inherent in existing instruments for NIRF IGS while aspiring to the advantages of natural vision systems like the morpho butterfly eye, I have developed a new imaging system that replaces conventional voltage-domain image sensors with a unique asynchronous time-domain image sensor. The issue of high dynamic range is mitigated in two ways: (1) by using a time-domain pixel design that essentially permits individual pixels to dynamically select an integration time appropriate for the lighting conditions and (2) by using an asynchronous system design that allows each pixel to independently report values using an address-event representation readout scheme. Sensitivity to both visible light and NIR light as well

as elimination of temperature-dependent co-registration error is accomplished by monolithically integrating the image sensor with four types of pixelated interference filters. These filters are tuned for high transmission over the blue, green, red, and NIR spectra and for high optical densities outside of these spectral bands. This architecture enables a single-chip snapshot multispectral imaging system that exhibits a dynamic range of ~120 dB and a maximum signal-to-noise ratio of ~56 dB. The imaging system is capable of imaging clinically relevant concentrations of less than 100 nM of the FDA-approved NIRF dye ICG.

1.3 The Structure of This Thesis

The main content of this thesis is divided into two chapters. In Chapter 2, the dynamic range of the surgical site in the operating room is explored in detail, and a lower bound is established on the dynamic range induced by the light sources used in NIRF IGS and the basic properties of biological tissue. In Chapter 3, a bio-inspired, asynchronous, time-domain, multispectral imager is presented that provides the high dynamic range, minimal co-registration error, compact size, and low cost demanded by NIRF IGS, and the imager is evaluated to demonstrate its high compatibility with NIRF IGS.

CHAPTER 2   AN ANALYSIS OF THE DYNAMIC RANGE OF THE OPERATING ROOM

2.1 Origin of the High Dynamic Range

In NIRF IGS, the surgical site is illuminated with both visible light and NIR light, and a special camera captures co-registered images that depict the gross anatomy and the location and shape of specific structures (e.g., tumor tissue). An overview of this imaging setup is provided in Figure 2.1. On the one hand, the visible light that is produced by surgical lamps will simply reflect off the tissue and be collected and registered by the camera. On the other hand, the NIR light that is often generated by narrowband LEDs or beam-expanded lasers must transmit into and scatter through the tissue, excite the fluorophore, and scatter through and transmit out of the tissue to be collected. An outline of the optical paths experienced by the light is provided in Figure 2.2. The differences in the light sources used to illuminate the patient and the fluorophores and the asymmetries in the optical paths experienced by the visible light and the NIR light conspire to create a high dynamic range scene. In this scene, the visible signal that merely provides the context of the surgical site is very strong and the NIR signal that actually demarcates the relevant structures is very weak. If a single image sensor is used to visualize both the visible reflection and the NIR emission, the image sensor must support a sufficiently high dynamic range between the color channels and the NIR
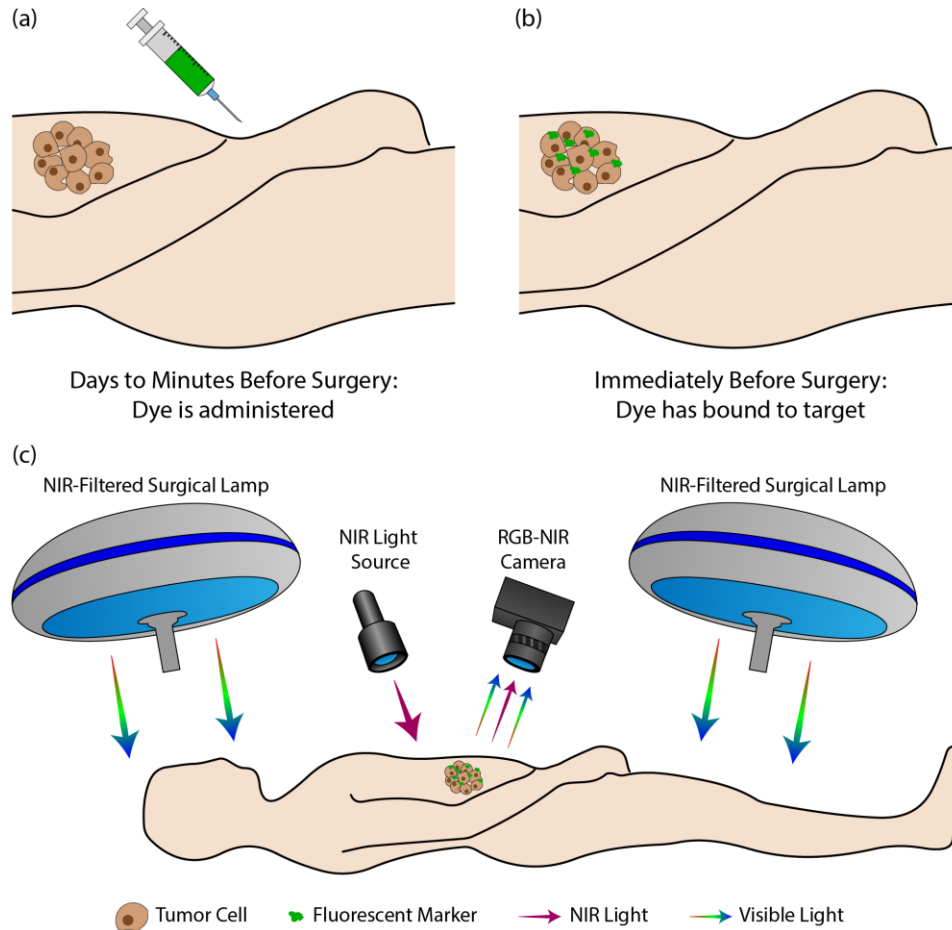
Figure 2.1: Overview of the imaging setup for NIRF IGS. (a) State of surgical site days to minutes before surgery when dye is administered. (b) State of surgical site immediately before surgery when dye has bound to target. (c) Configuration of light sources and camera during surgery.

channel. Otherwise, the surgical environment must be modified, or the image quality will suffer. Since these two options unacceptably impede the surgical workflow during demanding procedures, it is important to quantify the difference between signals and verify that sensors are compatible.

In general, the physical models of the light-tissue interaction that are required for an accurate computation of the dynamic range are very complex, and ongoing research is being conducted towards applying these models to this problem. Fortunately, though, simple computations can facilitate a rough bound on the dynamic range that indicates that most cameras are incapable of being used for NIRF IGS. These computations involve the determination of the

7
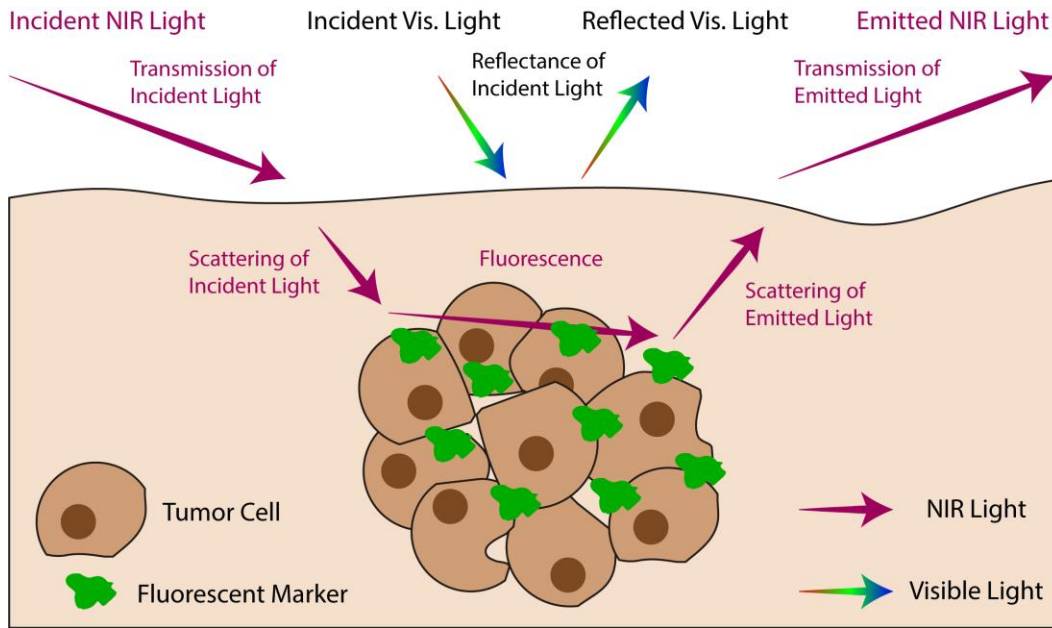
Figure 2.2: Optical path experienced by visible light and NIR light during NIRF IGS.

photon fluxes produced by the light sources and the contributions of these photon fluxes to meaningful signal at the image sensor, and they are outlined over the next few sections.

Before commencing this discussion, it is worth noting that there are many factors that contribute to the dynamic range of the operating room, and by properly selecting these factors, it is possible to develop a model where the dynamic range is arbitrarily high. To guide this analysis towards meaningful conclusions, the assumptions have generally been selected to determine a best-case dynamic range. To make this discussion even more concrete, we will consider the use of commercially available surgical lamps for visible illumination and the use of a 780 nm beam-expanded laser for NIR excitation. This configuration is similar to the NIRF IGS setup used for sentinel lymph node mapping with the fluorescent dye ICG, which represents a very realistic scenario.

2.2 Determining the Photon Fluxes from Light Sources

While federal agencies such as the US FDA reserve the right to control the distribution and application of medical devices, these agencies rely on international standards to define the

technical requirements that manufacturers must follow [20]–[22]. The International Electrotechnical Commission (IEC) has published a variety of standards including relevant standards for NIRF IGS that describe the general-purpose surgical lighting needed to illuminate patients during surgery and the NIR LED/laser sources needed to excite fluorophores during imaging. In IEC 60601-2-41, the IEC specifies the brightness and spectrum that surgical lamps must provide to be used in the operating room. In particular, surgical lamps must provide an illuminance between 40 klx and 160 klx, a color temperature between 3,000 K and 6,700 K, and a color rendering index between 85 and 100 [23]. In IEC 60825-1, the IEC specifies that the irradiance of NIR LED/laser sources must be kept below a lower threshold to be eye-safe (i.e., to be used without safety glasses) and a higher threshold to be skin-safe (i.e., to be used without skin protection) with the two thresholds varying as a function of the wavelength. For example, a 780 nm LED/laser source that has been sufficiently expanded must provide an irradiance below 54.85 mW/cm^2 to be eye-safe and an irradiance below 289.09 mW/cm^2 to be skin-safe [24]. Taken together, these requirements specify the illumination conditions present in the operating room, and they can be used to derive quantities needed to compute the dynamic range. To promote a best-case analysis, the gap between the visible lighting and the NIR lighting will be narrowed by considering the visible illumination at its minimum permissible value of 40 klx and the NIR illumination at its maximum permissible value of 289.09 mW/cm^2.

2.2.1 Properties of Visible Illumination

To compute the number of photons generated by a surgical lamp, it is necessary to know the spectrum of the surgical lamp. Historically, surgical lamps utilized incandescent bulbs with broad spectra produced via blackbody-like emission ranging from the visible spectrum into the infrared spectrum. Unfortunately, though, these bulbs generated a large amount of radiated heat and exploded unpredictably upon failure, risking burns to and contamination of the surgical area. As a

result, modern surgical lamps have shifted to LED bulbs that produce white light by mixing the spectral contributions of a narrow-band blue LED and a broader-band yellow phosphor. To the benefit of surgeons and patients alike, these bulbs produce very little heat, do not catastrophically fail, and generally offer greater flexibility in spectral response.

To compute the photon flux of an older lamp, it is assumed that the surgical lamp uses an incandescent bulb with a color rendering index of 100 and a color temperature of 4,000 K, and to compute the photon flux of a newer lamp, it is assumed that the surgical lamp uses a white LED with a color rendering index of 90 and a color temperature of 4,000 K. In both cases, the area of illumination is assumed to be circular with a 22.86 cm diameter. Determined from an extensive market evaluation, these values are both consistent with commercial systems and compliant with international standard [25]. Computing the spectrum of a blackbody radiator at the appropriate temperature in the former case [26] and using a representative spectrum generated from commercial components in the latter case [27], [28], it is possible to predict the normalized spectrum of the lamp, and scaling this spectrum to achieve a target illuminance over the surgical field, it possible to compute the spectral radiant flux density of the light bulb in watts per meter squared per nanometer. Determining the energy of a photon at each wavelength using the Planck-Einstein relationship and dividing the spectral radiance through by the energy per photon, it is possible to compute the spectral photon flux density in photons per second per meter squared per nanometer. By computing the integral under and the average of the spectral photon flux density, it is possible to compute the total photon flux density and the average wavelength across the visible spectrum. For an illuminance of 40 klx, this corresponds to a total photon flux density of $\sim 4.39 \times 10^{16}$ ph·s^{-1}·cm^{-2} and an average wavelength of ~569 nm for an incandescent bulb and to a total photon flux density of $\sim 3.81 \times 10^{16}$ ph·s^{-1}·cm^{-2} and an average wavelength of ~570 nm

for a white LED. As should be expected, these two light sources are very similar in important properties, so without loss of generality, the results for the white LED will be used in further computations since they are more relevant to conventional surgeries.

2.2.2 Properties of NIR Excitation

To compute the number of photons generated by the laser source, straightforward computations are required. Knowing that the wavelength of the laser source is 780 nm, the energy of each photon can be computed using the Planck-Einstein relationship, and knowing that the irradiance of the laser source is 289.09 mW/cm^2, the photon flux density can be computed by division. Ultimately, this corresponds to a photon flux density of $\sim 1.14 \times 10^{18}$ ph·s^{-1}·cm^{-2} at a wavelength of 780 nm.

2.3 Modeling the Optical Paths of Light

When the visible light and the NIR light interact with the tissue before collection at the camera, a few basic optical processes will determine how much optical power is lost and how much is sensed. Among these processes are reflection and transmission at the air-tissue boundary, absorption and scattering within the tissue, and fluorescence due to the fluorophore.

2.3.1 Reflection and Transmission

At the boundary between the air and the tissue, light will undergo both reflection and transmission due to the impedance mismatch between the two materials. In the case of reflection, a fraction of the light that is incident on the boundary will be redirected into the incident medium, while in the case of transmission, a fraction of the light will be transferred into the emergent medium. Both phenomena are predicted by the Fresnel equations which state that the reflectance R, the ratio of light redirected backwards, and the transmittance T, the ratio of light transported forwards, are given by

$$R = \left|\frac{n_1 - n_2}{n_1 + n_2}\right|^2 \text{ and } T = 1 - R \tag{2.1}$$

where n_1 is the refractive index of the incident medium, n_2 is the refractive index of the emergent medium, and the incident angle is $90°$ [29].

In reality, there may be other boundaries within the tissue, such as boundaries between tissue types, where reflection and transmission will occur. For the most part, the variation in refractive index within the tissue will be smaller than the sharp change in refractive index at the air-tissue boundary, so reflections will be correspondingly smaller. However, additional reflections in the visible spectrum will increase the measured intensity by giving transmitted light a second chance to reach the camera, while additional reflections in the NIR spectrum will decrease the measured intensity by redirecting light along paths that do not reach the fluorophore or the camera. Consequently, these additional boundaries will be neglected in an effort to find the best-case dynamic range so that the visible signal is minimized and the NIR signal is maximized.

2.3.2 Absorption and Scattering

Throughout the bulk of the tissue, light will undergo absorption and scattering due to the interaction of the photons with the tissue. In the case of absorption, photons are consumed when energy is transferred to the tissue and dissipated as heat, and in the case of scattering, the paths of photons are modified due to gradients in the refractive index of the tissue. Both phenomena are predicted by the Beer-Lambert Law which states that the transmittance T, the ratio of light that is neither absorbed nor scattered, is given by

$$T = e^{-(\mu_a + \mu_s)\ell} \tag{2.2}$$

where μ_a is the absorption coefficient of the tissue, μ_s is the scattering coefficient of the tissue, and ℓ is the thickness of the tissue [29].

While this equation implies a symmetry between absorption and scattering, an important distinction should be made: Absorption results in the actual loss of photons, whereas scattering results in the mere redirection of photons. Consequently, absorbed photons will never contribute to a signal, but scattered photons could be collected by an imaging array during data capture. However, the scattering of light results in the loss of spatial information which produces image blur and other detrimental effects, so deep tissue imaging techniques remove these scattered photons using spatial filtering [30]. As a result, these scattered photons will be eliminated from the computations, and absorbed photons and scattered photons will be treated on equal footing.

2.3.3 Fluorescence

In the presence of a fluorophore, light at one wavelength may excite the fluorophore and cause it to emit light at another wavelength during the process of fluorescence. In general, fluorescence is a complicated non-linear optical process that involves a stochastic interaction between the fluorophore and a collection of photons and phonons. However, in many cases, it is sufficiently described by a simple statistical model: When a photon is absorbed by the fluorophore, a fluorescent photon is generated with some probability described by the *quantum yield* Φ of the fluorophore.

Unfortunately, this simplification does not address two complexities. First, fluorophores exhibit finite absorption coefficients, so light will be absorbed within finite volumes of tissue and not at individual points in the tissue. Since a best-case approximation of the dynamic range is required and a finite absorption coefficient increases the dynamic range by weakening the NIR signal, this complexity is mitigated by assuming an infinite absorption coefficient so that all excitation photons are consumed and any emitted photons are generated at the boundary between the tissue and the fluorophore. Second, the propagation directions of fluorescent photons will be determined by the orientation and the organization of the fluorophores, so the resultant distribution

13

of propagation directions could range from very anisotropic if the fluorophores are highly structured to very isotropic if the fluorophores are randomly ordered. To incorporate this effect using a physically meaningful approximation, it is expected that the fluorophores are arbitrarily oriented so that they emit isotopically, and it is assumed that the only photons reaching the camera are those emitted in a cone that extends from the fluorophore to the camera. To model this process, a quantity called the *collection efficiency* C is defined that represents the fraction of fluorescent photons that the camera collects and is computed by dividing the solid angle accepted by the camera with the solid angle of a sphere. If the camera and the fluorophore are separated by a long distance as is necessary during surgery, the emitted light must be nearly parallel to the axis between the camera and the fluorophore to be collected, so the solid angle subtended by the narrow cone between the two is used to compute the collection efficiency.

2.4 Computing the Dynamic Range

With the properties of the light sources and the optical paths determined, it is possible to compute the dynamic range in the operating room. The dynamic range DR is defined as the ratio of the maximum intensity $I_{\max}$ and the minimum intensity $I_{\min}$ present in the scene:

$$DR = I_{\max}/I_{\min} \tag{2.3}$$

The maximum intensity $I_{\max}$ is defined by the visible illumination $I_{\mathrm{out,vis}}$ that reaches the camera. This value is determined by the light intensity $I_{\mathrm{in,vis}}$ produced by the surgical lamps as well as the reflectance $R_{\mathrm{vis,air\text{-}to\text{-}tis}}$ at the tissue-air boundary. It is computed as

$$I_{\mathrm{out,vis}} = R_{\mathrm{vis,air\text{-}to\text{-}tis}}I_{\mathrm{in,vis}} \tag{2.4}$$

The minimum intensity $I_{\min}$ is defined by the NIR illumination $I_{\mathrm{out,nir}}$ that reaches the camera. This quantity is determined by the light intensity $I_{\mathrm{in,nir}}$ produced by the laser source as well as the transmittance $T_{\mathrm{nir,air\text{-}to\text{-}tis}}$ across the air-tissue boundary, the transmittance $T_{\mathrm{nir,to\text{-}fluor}}$ through the

14

tissue to the fluorophore despite absorption and scattering, the quantum yield Φ of the fluorophore, the transmittance $T_{\text{nir,from-fluor}}$ from the fluorophore through the tissue despite absorption and scattering, the transmittance $T_{\text{nir,tis-to-air}}$ across the tissue-air boundary, and the collection efficiency C of the lens.

$$I_{\text{out,nir}} = CT_{\text{nir,tis-to-air}}T_{\text{nir,from-fluor}}\Phi T_{\text{nir,to-fluor}}T_{\text{nir,air-to-tis}}I_{\text{in,nir}} \tag{2.5}$$

Therefore, the dynamic range can be written as

$$DR = \frac{I_{\text{out,vis}}}{I_{\text{out,nir}}} = \frac{R_{\text{vis,air-to-tis}}I_{\text{in,vis}}}{CT_{\text{nir,tis-to-air}}T_{\text{nir,from-fluor}}\Phi T_{\text{nir,to-fluor}}T_{\text{nir,air-to-tis}}I_{\text{in,nir}}} \tag{2.6}$$

where the various parameters are functions of the tissue, the fluorophore, and the imaging setup.

The reflectances and transmittances at the boundaries can be determined from the refractive indices of the air and the tissue, and the transmittances through the tissue can be determined from the absorption coefficient, the scattering coefficient, and the depth of the tissue. In general, the refractive indices and various coefficients are functions of the wavelength. For simplicity, though, it is assumed that the wavelength of the visible illumination is the average wavelength computed from the surgical lamp, and it is assumed that the wavelength of the NIR illumination is the excitation wavelength of the laser source. Since the optical properties of many tissues do not vary extensively across the visible spectrum or between the excitation wavelength and the emission wavelength in the NIR spectrum (for reasonably small Stokes shifts), this is a reasonable assumption. As an example, we can consider adipose tissue which has a refractive index of 1.478 at 570 nm, a refractive index of 1.469 at 780 nm, an absorption coefficient of 1.01 cm^{-1} at 780 nm, and a scattering coefficient of 11.16 cm^{-1} at 780 nm [31], [32]. Using a refractive index of unity for air, the reflectances and transmittances can thus be determined as a function of tissue depth. The quantum yield is computed from measurements of real fluorophores, and for ICG, it takes a
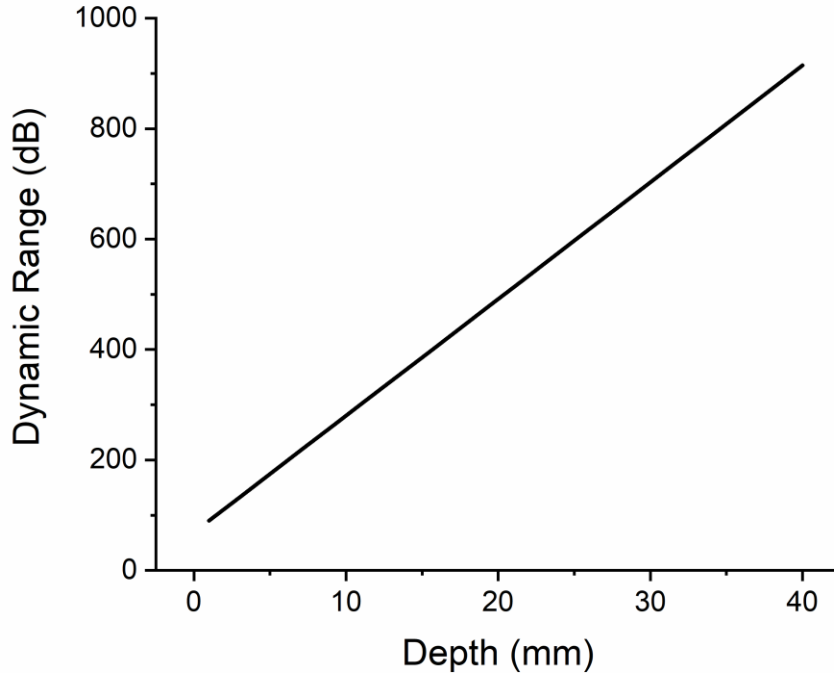
Figure 2.3: Dynamic range needed to capture both the visible signal generated by light reflection from tissue and the NIR signal generated by fluorescent emission from fluorophore at different depths. The light sources that are simulated are modeled on realistic surgical lamps and laser sources, and the tissue optics are modeled on adipose tissue.

value of 2.58% [33]. The collection efficiency is determined from the geometry of the imaging setup, but for large distances between the tissue and the camera, it can be computed for a narrow cone with a sufficiently small subtended angle (e.g., 1 degree).

By sweeping the depth of the tissue and computing the dynamic range at each depth using the equations and quantities described in this section, a plot of dynamic range versus tissue depth can be generated. As shown in Figure 2.3, this analysis indicates that a dynamic range of ~90 dB is needed for a fluorescently labeled structure at the surface of the tissue, and the dynamic range only increases for larger depths. This result proves troubling in light of the optoelectronic characterization of state-of-the-art imagers: Most sensors exhibit dynamic ranges that are bounded to 80 dB which is well short of the best-case dynamic range of ~90 dB required for NIRF IGS

[34]. Provided that surgical lighting is not dimmed during the operation of these cameras, it is likely that these systems are capturing sub-optimal images and are missing critical detail in the NIR channel. To ensure that the full extent of fluorescently labeled structures is detected, it is necessary to use alternative architectures for imaging sensors that push the available dynamic range beyond that required in application.

CHAPTER 3   A BIO-INSPIRED, ASYNCHRONOUS, TIME-DOMAIN MULTISPECTRAL IMAGING SYSTEM

3.1 Issues with Reducing the Dynamic Range of the Scene

To combat the high dynamic range of the operating room, there are a few different options, but if the fluorescent signal is too weak, it is reasonable to search for ways to improve the fluorophore providing the signal. Days to minutes before surgery using NIRF IGS, this fluorophore is administered such that during surgery a greater concentration of fluorescent molecules will be found in tumor cells than in surrounding tissue. The duration and location of the administration process is determined by the molecular marker's type and its kinetics. For untargeted molecular markers, the distribution of the dye may be dictated by the enhanced permeability and retention effect, a phenomenon in which small molecules are accumulated and retained in tumors due to the dense and disorderly vasculature and the sparse lymphatics associated with tumor growth [35]. For targeted molecular markers, fluorescent molecules are conjugated to special structures so that the composite probe can preferentially target tumor characteristics such as increased glucose uptake and elevated growth factor interaction [36], [37]. Depending on the binding behavior and the hydrodynamic size of the probes, molecular markers may be cleared by the kidney, the liver, or other pathways over time frames of varying length, and this clearance behavior will determine whether local injection is required or whether global administration can be tolerated [38]. As long

as proper procedures are followed, tumors can be highlighted at any location in the body, meaning that fluorescent signals can originate from deep within tissues.

A variety of fluorescent dyes have been proposed and examined by both academics and companies alike. Early applications relied on the surgeon's eyes to discriminate the fluorescent signal from the background scene, so fluorescent dyes with visible emission were required. Fluorescein sodium, the chemical used in the first instances of nontargeted and targeted fluorescence surgical imaging, has been used in the visualization of brain tumors and colorectal tumors, and 5-aminolevulinic acid, a precursor that stimulates the *in vivo* production of the fluorescent molecule protoporphyrin IX, has been explored as an option for a variety of central nervous system tumors [6]. While providing a major benefit in terms of surgical complexity by eliminating the need for a separate imager, visible fluorophores are ultimately limited in efficacy by the high absorption coefficient, scattering coefficient, and autofluorescence exhibited by tissues in the visible spectrum, factors that limit the contrast between the fluorescence and the background [39].

As a result, most research has turned to the development of fluorescent dyes with NIR emission. The two fluorescent markers that have been approved by the US FDA, MB and ICG, are untargeted compounds that received approval before the advent of fluorescence imaging but have found applications ever since for their track record of safety and NIR emission. MB, a dark blue chemical with 680 nm fluorescence, was used for many years as a visible contrast agent and has been used more recently for the localization of pancreatic tumors, and ICG, a dark green chemical with 820 nm fluorescence, has been used to study blood perfusion and to locate sentinel lymph nodes [40]. In the hopes of boosting the quantum yield, increasing the spectral performance, and

improving the overall flexibility of fluorescent dyes, a variety of other chemicals are being explored, but none have been approved for clinical use.

Due to the factors that have been discussed, the potential depth of tumor tissue, the optical properties of intervening tissue, and the limitations on the availability of fluorescent dyes place a limit on the imaging performance possible in the operating room. Any imaging system must be designed to overcome these limitations in order to provide high-quality images in a practical package.

3.2 Techniques to Increase the Dynamic Range of the Sensor

The dynamic range of an image sensor is computed as the ratio of the maximum measurable signal to the minimum measurable signal which correspond to the measurements under very strong illumination and very weak illumination, respectively. For ordinary CMOS image sensors, the factors that determine the dynamic range are well understood. Under strong illumination, the dynamic range is limited by the maximum photocharge that can be accumulated on the photodiode which is in turn determined by the reset voltage and the junction capacitance. Assuming that the fabrication process is fixed, this relationship means that the dynamic range can be improved by either increasing the reset voltage or increasing the photodiode area; however, power consumption and area requirements as well as absolute maximum voltage thresholds practically limit the potential for improvement. Under weak illumination, the dynamic range is generally limited by the reset noise and the readout noise which can be reduced with correlated double sampling and other noise-sensitive techniques. If noise sources are sufficiently minimized, though, the minimum signal may become a single electron—imposing a fundamental limit on the dynamic range. As a result, most techniques for extending the dynamic range focus on boosting the maximum

detectable signal since it can theoretically be increased without bound instead of reducing the minimum detectable signal since it is limited by physics.

To overcome the firm bounds on the dynamic range of conventional CMOS image sensors, researchers have sought simple modifications to the standard pixel structure to extend the dynamic range in other ways. Well adjustment and multiple sampling have been popular approaches since the only changes that are needed are changes to the peripheral circuitry that controls the reset and readout of the pixel array [41].

In well adjustment sensors, the gate voltage of the reset transistor is modulated from a large value to a small value during the integration time, causing the potential barrier between the photodiode and the supply to vary from a small value to a large value and inducing a corresponding increase in the well capacity with time [42]. In low light conditions, the accumulation of photocharge will be slower than the growth in the well capacity, leading to a normal change in the photovoltage, but in high light conditions, photocharge will accumulate faster than the well capacity grows, causing the excess photocharge to spill over into the supply and enforcing a ceiling on the photovoltage. By properly controlling the well capacity, a non-linear transfer function from photocurrent to photovoltage can be created that can artificially compress the dynamic range of the scene and increase the dynamic range of the image. While the implementation is relatively straightforward since a single voltage is swept with time, a theoretical decrease in signal-to-noise ratio and a practical increase in noise due to the well adjustment pose a risk of degradation of small signals.

In multiple sampling sensors, the non-destructive measurement of the photocharge on the photodiode is exploited to enable multiple readouts of the image sensor within a single integration time [43], [44]. Since low light pixels will saturate slowly while high light pixels will saturate

quickly, it is likely that every pixel will be well exposed in at least one frame from these multiple exposures, so pixel-level or image-level exposure fusion can be used to combine these low dynamic range frames to produce a single high dynamic range image. Although exposure fusion promises to increase signal-to-noise ratio through temporal averaging, the implementation of the full system is difficult since a high-speed readout chain is required to support sequential measurements and sufficient logic and memory are required for real-time image processing.

To overcome the inherent difficulties that are present in man-made designs, attention has been drawn to natural vision systems that exhibit high dynamic ranges and robust operation, and experts have tried to reproduce this biological performance with electronic circuits. These so-called neuromorphic architectures trace back to the synthetic retina developed by Mead and Mahowald that reproduced the complex of photoreceptor cells, horizontal cells, and bipolar cells entwined in the human eye with a network of photodetectors, transistors, and resistors implemented *in silico* [45]. While this chip succeeded at its mimicking act so well that it suffered from optical illusions, it found little traction in actual application due to its impractical architecture [46]. Nonetheless, its success at mapping biological structures to electronic networks has served as the inspiration for many technologies that aim to make the imaging process more adaptive and more efficient [47].

A common approach to this task replaces the linear response of an ordinary photodiode with the logarithmic response observed in many animals [48]. By pairing a reverse-biased photodiode capable of converting a photon flux into a photocurrent and a sub-threshold transistor capable of converting a linearly varying photocurrent into a logarithmically varying photovoltage, a logarithmic readout can be induced with few modifications to standard pixels. Although this

technique is successful at extending the dynamic range of image sensors, workarounds are required to mitigate the high sensitivity to device mismatch cause by sub-threshold operation.

A different approach attempts to encode light intensity not in the absolute magnitude of a voltage signal across a photodiode but in the relative frequency of voltage pulses, thereby simulating neuron-to-neuron communication [49]. By comparing the voltage across a photodiode with a fixed threshold and resetting the photodiode when the threshold is surpassed, an intensity signal can be encoded in the reset signal: When the light is bright, the voltage will decay to the threshold quickly, causing an increase in the reset rate of the pixels due to an increase in the frequency of the reset signal, but when the light is dim, the voltage will decay to the threshold slowly, leading to a low pixel reset rate and slow reset signal frequency. However, the delay lines needed to generate the reset signals lead to high pixel-to-pixel mismatch in the output frequencies that are harder to calibrate than ordinary fixed pattern noise.

While these more practical image sensors suffer from a variety of issues, they are further limited by a synchronous readout scheme in which rows and columns are read out one by one at a fixed rate. In contrast, natural vision systems are constantly measuring the light intensity and adapting to the scene. With the introduction of the address-event representation into the sensing literature, a new breed of image sensors closed this gap by implementing pixels that independently detect light intensity and asynchronously report measurements to a central controller. With the development of the dynamic vision sensor (DVS) by Lichtsteiner et al. [50] and the asynchronous, time-based image sensor (ATIS) by Posch et al. [51], the performance of natural vision systems and the practicality of man-made camera systems were married, producing imagers that exhibit both high dynamic range and high signal-to-noise ratios due to the pixel-level adaptation of the imaging process while retaining compatibility with standard digital signal processing workflows.

Due to these features, they show great promise for imaging applications in demanding environments, and they have served as a basis for a new imaging sensor for NIRF IGS.

3.3 A Multispectral Imager for High Dynamic Range Imaging

In light of the observations that have been presented over the past few chapters and sections, I have developed a new imaging system for NIRF IGS that is aimed at solving the practical issues in the operating room. At the heart of this imaging system is an asynchronous time-domain image sensor that enables simultaneous imaging of very bright and very dim channels. As shown in Figure 3.1, it combines time-domain pixels and additional logic as part of an asynchronous system that reports pixel values to an image processor as they become available, eliminating the need for a fixed integration time and frame rate. This image sensor is integrated with pixelated interference filters to enable simultaneous imaging of both color and NIR channels at high dynamic range and without temperature-dependent co-registration error.

The pixel architecture was developed to free the pixel from the dynamic range constraints imposed by a fixed integration time [52]. In a traditional voltage-domain pixel, a capacitor is reset to a known voltage at the beginning of each integration period, and the voltage remaining on the capacitor after accumulation of photoelectrons is measured at the end of each integration period. In the time-domain pixel used in this imager, though, pixels no longer report the voltage after a fixed integration time but instead report the time at which the voltage exceeds certain thresholds. While a single threshold can be used as illustrated in Figure 3.2a and Figure 3.2b, reset noise can be eliminated through correlated double sampling if every pixel reports the times at which the voltage exceeds a high threshold and a low threshold and the system measures the difference between the times. This functionality is accomplished using the circuit shown in Figure 3.2c. The n-well/p-sub photodiode PD and the reset transistor M_1 provide a photovoltage that is compared
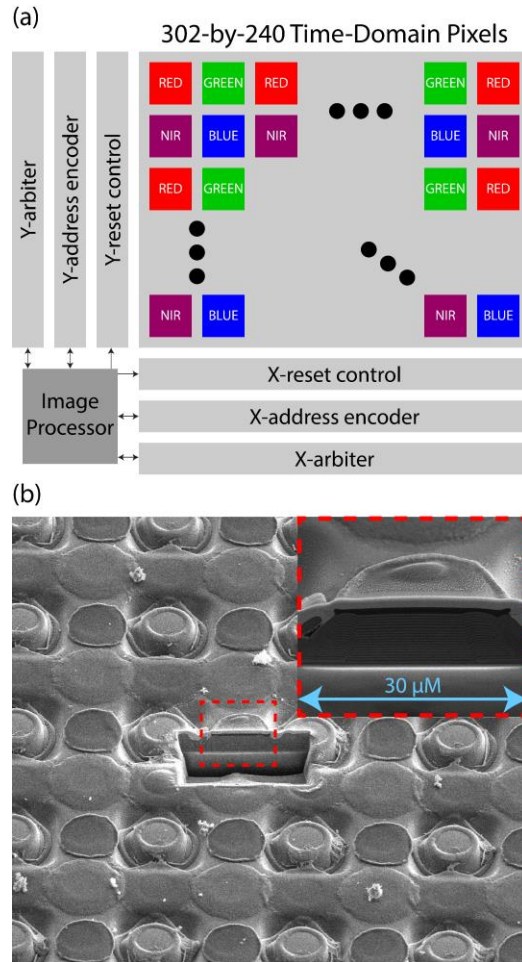
Figure 3.1: (a) Block diagram of the sensor's architecture. The pixelated interference filters are monolithically integrated with the time-domain pixels for multispectral discrimination. The pixels communicate with the arbiters, encoders, and controllers at the periphery of the imaging array which pass pixel data to the image processor. (b) Cross-sectional scanning electron microscope image of the pixelated interference filters. Many thin film layers with different dielectric constants are used to tune the spectral response and increase the optical density of the stop bands. [© 2018 IEEE]

to a reference voltage using the two-stage comparator formed by $M_2 - M_6$ and by M_7 and M_9.

Hysteresis is provided by M_{10} and M_{11}, providing noise immunity that prevents glitches at the

output, and power reduction is provided by M_8, shutting off current in the second stage when the

voltage threshold has been exceeded in the first stage. When the pixel is reset, the threshold voltage

is set to a high reference voltage; when the high reference voltage has been exceeded, the threshold

voltage is set to a low reference voltage; and when the low reference voltage is exceeded, the pixel
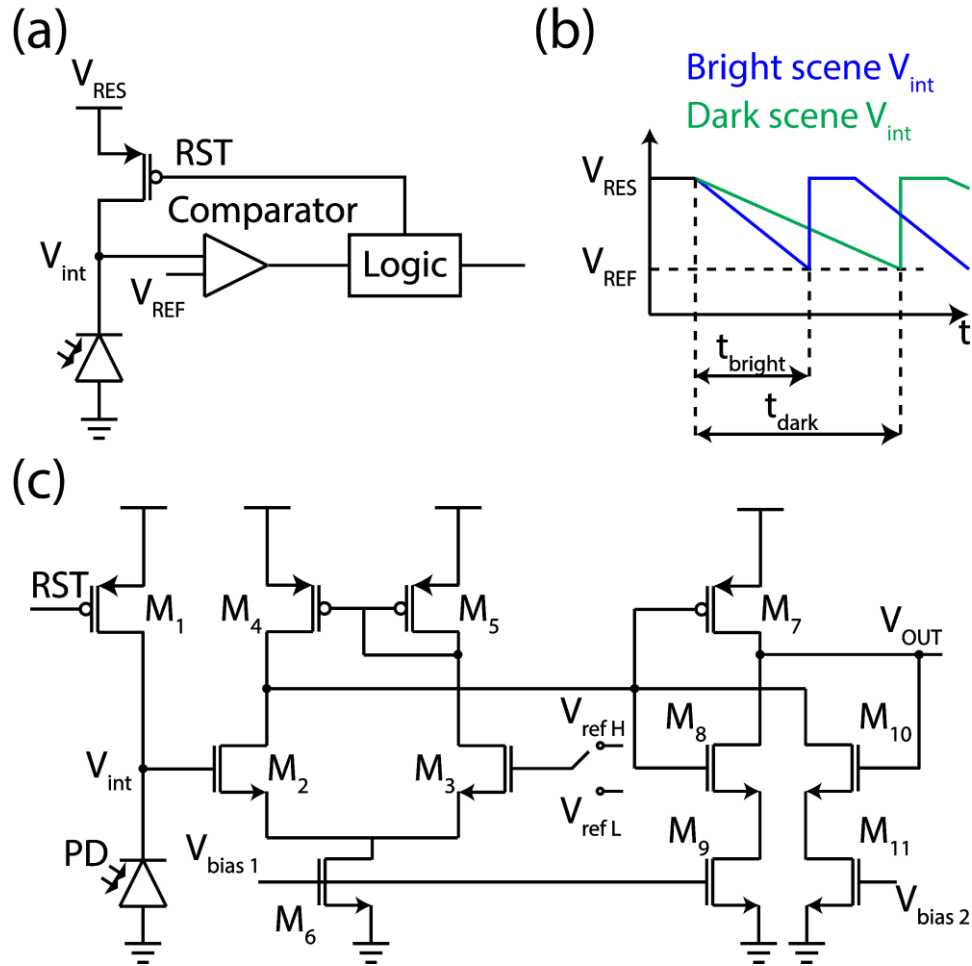
Figure 3.2: (a) Example of a time-domain pixel with a single threshold voltage. (b) Time diagram of the example pixel's response to bright and dark scenes. (c) Schematic of the time-domain pixel with two threshold voltages used in this image sensor. [© 2018 IEEE]

enters an idle state. When the voltage exceeds either threshold, an exposure event occurs at the output that triggers system logic responsible for measuring pixel values. The pixels were placed with a pitch of 30-by-30 µm and exhibited a fill factor of 20%.

The system architecture was developed to permit individual pixels to independently and asynchronously report their values [53]. It consists of a 302-by-240 pixel array as well as the necessary address-event representation logic to permit every pixel to request global resources and transmit values using a four-phase handshake protocol. The structure of the system is shown in the block diagram in Figure 3.1a. When a pixel undergoes an exposure event, i.e., discharging below

the high threshold voltage or low threshold voltage, the pixel begins negotiations with two arbitration and encoding units. First, the pixel pulls down the "Y-Request" row bus and waits for a response on the "Y-Acknowledgement" row bus indicating that the row address of the pixel has been encoded. Second, the pixel pulls down the "X-Request" column bus and waits for a response on the "X-Acknowledgement" column bus indicating that the column address of the pixel has been encoded. If multiple pixels in a row request row address encoding simultaneously, their row addresses and column addresses will be encoded at the same time, reducing the demand on the arbiters and ensuring system responsiveness. When both addresses are encoded, the complete address is transmitted to an off-chip processor that logs the address and the timestamp of the event, and the pixel can be reset for the next exposure. The full system was implemented using a standard 180 nm mixed-signal CMOS process on a 9.9-by-8.2 mm die with a 77%/23% split between the active area and support circuitry. Timestamps are generated using a 1 MHz counter that provides 1 µs resolution, and facilities are provided for tuning the threshold voltages to optimize performance.

To provide spectral discrimination across three color channels and an NIR channel, the pixel array was monolithically integrated with a pixelated filter array constructed from a repeating 2-by-2 pixel pattern of blue, green, red, and NIR interference filters. An SEM image of the pixelated filter array is shown in Figure 3.1b. The interference filters were fabricated via physical vapor deposition of multiple thin-film dielectric layers with different refractive indices. Using finite element methods, light propagation through the dielectric stack was simulated, and applying iterative optimization to select the materials, e.g., SiO_2 and TiO_2, as well as the number and thickness of the dielectric layers, passband shapes were tuned to provide a proper spectral response

27

for NIRF IGS and similar applications. This structure enables a single-chip snapshot multispectral imaging system that is free from temperature-dependent co-registration error.

3.4 Optoelectronic Characterization

In a traditional voltage-domain pixel, the dynamic range is limited by the voltage supply and the full well capacity on the high side and the reset noise and readout noise on the low side. As a result, dynamic ranges for conventional imagers are practically limited to between 65 and 80 dB [34]. In the time-domain pixel used in this imager, though, the dynamic range is limited by the shortest integration time possible (which occurs at maximum photocurrent) and the longest integration time possible (which occurs at minimum photocurrent when dark current dominates). Consequently, dynamic ranges up to 140 dB have been achieved with this pixel architecture, and a dynamic range of 120 dB was measured with this sensor [53]. As a side effect of this measurement scheme, the signal-to-noise ratio of the time-domain pixel differs from that of a voltage-domain pixel: Since every pixel is completely discharged regardless of photon flux, the signal-to-noise ratio at low and high light intensities alike is shot noise limited. As shown in the plot of signal-to-noise ratio in Figure 3.3d, this leads to a broad and flat region where the signal-to-noise ratio hovers near 56 dB for more than 4 decades of light intensities.

The quantum efficiencies of the color and NIR channels were measured by projecting the tunable narrowband output of a monochromator onto the imager and examining the response as the output was scanned across wavelengths. As shown in the plots of quantum efficiency and optical density in Figure 3.3a and Figure 3.3b, the blue, green, red, and NIR channels exhibit peak quantum efficiencies of ~3.4%, ~12.9%, ~16.5%, and ~12.9 % at 476, 559, 659, and 706 nm, respectively. The maximum in optical density observed at ~785 nm is attributed to a discrete laser
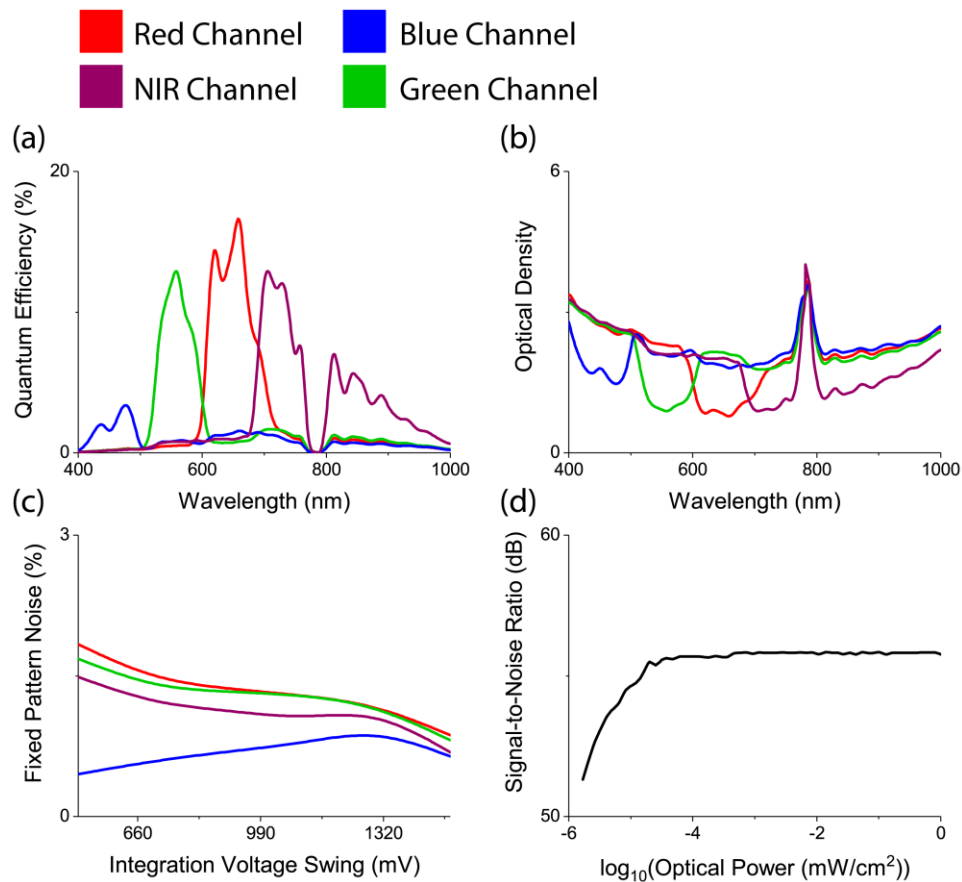
Figure 3.3: Optoelectronic characterization graphs of the imaging system. (a) Quantum efficiency. (b) Optical density. (c) Fixed-pattern noise. (d) Average signal-to-noise ratio across all channels. [© 2018 IEEE]

notch blocking filter located between the lens and the imager that is used to eliminate the strong excitation source used in NIRF IGS. In general, the quantum efficiencies are low because the imager was fabricated using a standard mixed-signal process and not a special image sensor process, meaning the efficiencies could be easily improved by substituting the optimized structures provided by a specialized process.

The fixed-pattern noise (FPN) of the color and NIR channels was measured by projecting the uniform broadband output from a halogen lamp coupled to an integrating sphere onto the imager and examining the variation in response across the area of the imager. To reduce the effects of FPN, the gains and offsets of every pixel were computed and applied as part of a flat field
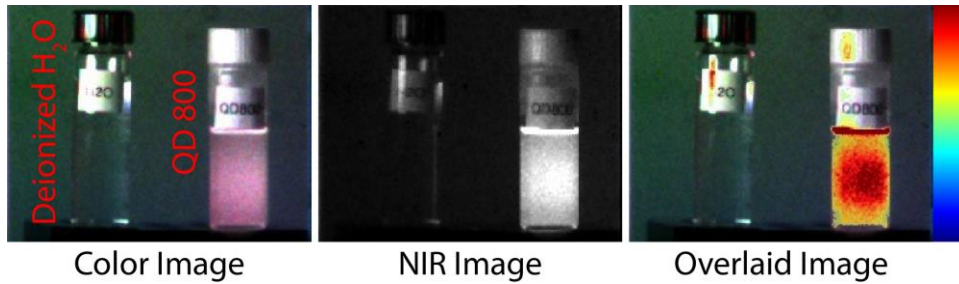
Figure 3.4: Sample images showing the color and near-infrared vision capabilities of the asynchronous time-domain image sensor. The scene contains two vials filled with deionized water (left) and QDot 800 (right). Left: Color image of the scene. Center: Near-infrared image of the scene. Right: Overlaid view of the near-infrared image in a false linear colormap and the color image. [© 2018 IEEE]

calibration algorithm. Figure 3.3c illustrates the FPN after calibration as a function of the difference between the high threshold and the low threshold at every pixel, i.e., the integration voltage swing. The FPN was bounded at less than 2% for all channels.

3.5 Near-Infrared Fluorescence Sensitivity

To illustrate the imaging system's capabilities, QDot 800, a solution of fluorescent quantum dots that absorbs photons at 780 nm and remits photons at 800 nm, was poured into a vial and imaged under surgical illumination produced by an LED panel and a 780 nm laser. A snapshot image of the vial of QDot 800 as well as a vial of deionized water is provided in Figure 3.4. While the color channels provide a good indication of where the vials are located, the NIR channel clearly distinguishes between the QDot 800, which provides substantial fluorescence signal, and the deionized water, which provides no fluorescence signal. Furthermore, the overlaid image where the color-mapped NIR channel and the color channel are superimposed indicates that the channels are spatially matched with no co-registration error.

To examine the camera's sensitivity to a clinically relevant fluorescent dye, the minimal detectable concentration of ICG was measured. Three serial dilutions of ICG in deionized water were produced at concentrations ranging from 10 mM down to 10 nM, and three additional samples

30

of deionized water were collected as control data. To mimic the ambient environment present during NIRF IGS, the three sets of solutions were imaged under 50 klx visible illumination from a custom LED panel and 20 mW/cm^2 NIR illumination from a filtered and diffused 780 nm laser. The pixel values across the three sets were clustered by concentration value to minimize error. The detection limit and the minimal detectable concentration were defined according to the International Union of Pure and Applied Chemistry (IUPAC) standard with a confidence level of 99.86% [54]. The minimal detectable concentration was found to be 100 nM which compares well with clinical dosages.

CHAPTER 4   CONCLUSION

4.1 Summary of This Work

NIRF IGS can provide surgeons with the information needed to identify tumor margins during surgical resection in real time, minimizing the need for costly and intensive follow-up treatments. Unfortunately, FDA-approved NIRF imaging systems suffer from issues with cost, size, limited dynamic range, and unpredictable co-registration error that have limited adoption. In this thesis, the dynamic range of a single-sensor camera that solves these problems was determined, and a novel imager based on the morpho butterfly's eye that meets this requirement was presented. This imaging system monolithically integrates an asynchronous time-domain image sensor and pixelated interference filters to provide three color channels and an NIR channel with a single-chip snapshot architecture. This imaging system provides a dynamic range of 120 dB and is free from temperature-dependent co-registration error. Furthermore, it can detect clinically relevant concentrations of FDA-approved NIRF dyes, making it a promising candidate for NIRF IGS applications.

4.2 Future Work

While the camera in this thesis has shown promise for NIRF IGS, there are several improvements that could be made and additional studies that could be run that would extend the system's performance and evaluate its efficacy.

4.2.1 Improvements to the Image Sensor Design

Since the image sensor in this imaging system was fabricated using a standard CMOS mixed-signal process instead of a specialized CMOS image sensor process, pixels were laid out with general-purpose silicon structures instead of the high-performance components seen in modern cameras. Consequently, a migration between processes would immediately present several opportunities for improvement. First, optimized photodiodes could be employed which would boost the quantum efficiency by better matching the depth of the depletion region to the location of the photocharge generation and expand the dynamic range by limiting the dark current produced at surface defects. Second, trench isolation could be implemented which would improve the optical density of the NIR channel by decreasing the electrical crosstalk from the visible pixels to the NIR pixels. Coupled with changes at the circuit level to improve the readout noise, these modifications would lower the smallest measurable NIR signal, pushing the minimum detectable fluorophore concentration lower and improving the detection of deep and diffuse tumor cells.

4.2.2 Improvements to the Signal Processing Pipeline

While the asynchronous event stream generated by this time-domain image sensor is substantially different from the synchronous rectangular images produced by conventional voltage-mode image sensors, the timestamps of events are ultimately discretized to a fixed frame rate and mapped to an ordinary image. As a result, there is an inherent inefficiency in the data processing pipeline since fluorophore detection must occur in a transformed measurement space instead of the original measurement space. At a more fundamental level, though, the conversion between domains could conceal information that is obvious in the events but is obscured in the images. For example, knowledge of temporal variations in the light source or the fluorophore emission may be easy to incorporate into a series of timestamps but may be difficult to apply to an array of grayscale values.

Therefore, a more cohesive workflow on the time-domain data could enable more efficient and more effective signal processing that could benefit system performance.

4.2.3 Additional Studies

While the measurement of the minimum detectable fluorophore concentration and the preliminary images from animal experiments appear promising, further work is required to verify this image sensor's usefulness for NIRF IGS. In particular, the generation of a receiver-operator curve for fluorophore detection in a mouse model would facilitate the prediction of system performance on larger populations, and the examination of fluorescently labeled tissues in human subjects would help to identify practical issues with system integration in the operating room.

REFERENCES

[1] S. Blair, M. Garcia, N. Cui, and V. Gruev, "A 120 dB, asynchronous, time-domain, multispectral imager for near-infrared fluorescence image-guided surgery," in *2018 IEEE Biomedical Circuits and Systems Conference (BioCAS)*, 2018, pp. 1–4.

[2] A. L. Luryi, M. M. Chen, S. Mehra, S. A. Roman, J. A. Sosa, and B. L. Judson, "Positive surgical margins in early stage oral cavity cancer," *Otolaryngol. Neck Surg.*, vol. 151, no. 6, pp. 984–990, Dec. 2014.

[3] M. S. Cookson and S. S. Chang, "Margin control in open radical prostatectomy: What are the real outcomes?" *Urol. Oncol. Semin. Orig. Investig.*, vol. 28, no. 2, pp. 205–209, Mar. 2010.

[4] B. A. Virnig, T. M. Tuttle, T. Shamliyan, and R. L. Kane, "Ductal carcinoma in situ of the breast: A systematic review of incidence, treatment, and outcomes," *JNCI J. Natl. Cancer Inst.*, vol. 102, no. 3, pp. 170–178, Feb. 2010.

[5] L. Jacobs, "Positive margins: The challenge continues for breast surgeons," *Ann. Surg. Oncol.*, vol. 15, no. 5, pp. 1271–1272, May 2008.

[6] A. L. Vahrmeijer, M. Hutteman, J. R. van der Vorst, C. J. H. van de Velde, and J. V. Frangioni, "Image-guided cancer surgery using near-infrared fluorescence," *Nat. Rev. Clin. Oncol.*, vol. 10, no. 9, pp. 507–518, Sep. 2013.

[7] M. Garcia, M. A. Zayed, K. Park, and V. Gruev, "Near-infrared angiography for critical limb ischemia in a diabetic murine model," *J. Biomed. Opt.*, vol. 22, no. 4, p. 046006, Apr. 2017.

[8] M. Garcia *et al.*, "Bio-inspired imager improves sensitivity in near-infrared fluorescence image-guided surgery," *Optica*, vol. 5, no. 4, p. 413, Apr. 2018.

[9] A. V. DSouza, H. Lin, E. R. Henderson, K. S. Samkoe, and B. W. Pogue, "Review of fluorescence guided surgery systems: identification of key performance capabilities beyond indocyanine green imaging," *J. Biomed. Opt.*, vol. 21, no. 8, p. 080901, Aug. 2016.

[10] M. Garcia, K. Kauffman, T. Davis, R. Marinov, and V. Gruev, "A 1280 by 720 by 3, 250 mW, 24 fps hexachromatic imager for near-infrared fluorescence image-guided surgery," in *2018 IEEE International Symposium on Circuits and Systems (ISCAS)*, 2018, pp. 1–5.

[11] S. L. Jacques, "Optical properties of biological tissues: A review," *Phys. Med. Biol.*, vol. 58, no. 11, pp. R37–R61, May 2013.

[12] S. B. Mondal *et al.*, "Binocular Goggle Augmented Imaging and Navigation System provides real-time fluorescence image guidance for tumor resection and sentinel lymph node mapping," *Sci. Rep.*, vol. 5, no. 1, Jul. 2015.

[13]   J. Withgott, "Taking a bird's-eye view…in the UV," *Bioscience*, vol. 50, no. 10, pp. 854–859, Oct. 2000.

[14]   H. H. Thoen, M. J. How, T.-H. Chiou, and J. Marshall, "A different form of color vision in mantis shrimp," *Science*, vol. 343, no. 6169, pp. 411–3, Jan. 2014.

[15]   J. M. Valeton and D. van Norren, "Light adaptation of primate cones: An analysis based on extracellular data," *Vision Res.*, vol. 23, no. 12, pp. 1539–1547, Jan. 1983.

[16]   W. H. Miller, G. D. Bernard, and J. L. Allen, "The optics of insect compound eyes," *Science*, vol. 162, no. 3855, pp. 760–767, Nov. 1968.

[17]   M. Srinivasarao, "Nano-optics in the biological world: Beetles, butterflies, birds, and moths," *Chem. Rev.*, vol. 99, no. 7, pp. 1935–1962, 1999.

[18]   W. H. Miller, "Ocular optical filtering," in *Comparative Physiology and Evolution of Vision in Invertebrates (Handbook of Sensory Physiology, Vol. 7/6/6A)*, 1st ed., H. Autrum, Ed. Springer, Berlin, Heidelberg, 1979, pp. 69–143.

[19]   J. Keat, P. Reinagel, R. C. Reid, and M. Meister, "Predicting every spike: A model for the responses of visual neurons," *Neuron*, vol. 30, no. 3, pp. 803–817, May 2001.

[20]   *Code of Federal Regulations Title 21 §878.4580: Surgical lamp*. United States: Code of Federal Regulations, 2018.

[21]   *Code of Federal Regulations Title 21 §1040.10: Laser products*. Code of Federal Regulations, 2018.

[22]   *Code of Federal Regulations Title 21 §1040.11: Specific purpose laser products*. Code of Federal Regulation, 2018.

[23]   International Electrotechnical Commission, "Medical electrical equipment - Part 2-41: Particular requirements for the safety of surgical luminaires and luminaires for diagnosis (IEC 60601-2-41:2000)," 2000.

[24]   International Electrotechnical Commission, "Safety of laser products - Part 1: Equipment classification, requirements and user's guide (IEC 60825-1:1993+AMD1:1997+AMD2:2001 CSV)," 2001.

[25]   Meditek, "Comprehensive review of the most popular surgical lights in Canada," 2017. [Online]. Available: https://www.meditek.ca/comprehensive-review-popular-surgical-lights-canada/. [Accessed: 19-Nov-2018].

[26]   R. A. Serway, C. J. Moses, and C. A. Moyer, *Modern Physics*, 3rd ed. Belmont, CA: Brooks/Cole—Thomson Learning, 2005.

[27]   Lumileds, "Luxeon 3030 2D line datasheet," 2018. [Online]. Available: https://www.lumileds.com/products/mid-power-leds/luxeon-3030-2d. [Accessed: 19-Nov-2018].

[28]   Lumileds, "Luxeon 3014 datasheet," 2018. [Online]. Available: https://www.lumileds.com/products/mid-power-leds/luxeon-3014. [Accessed: 19-Nov-2018].

[29]   B. E. A. Saleh and M. C. Teich, *Fundamentals of Photonics*, 2nd ed. Hoboken, NJ: Wiley-Interscience, 2007.

[30]   C. Dunsby and P. M. W. French, "Techniques for depth-resolved imaging through turbid media including coherence-gated imaging," *J. Phys. D. Appl. Phys.*, vol. 36, no. 14, pp. R207–R227, Jul. 2003.

[31]   I. Y. Yanina, E. N. Lazareva, and V. V. Tuchin, "Refractive index of adipose tissue and lipid droplet measured in wide spectral and temperature ranges," *Appl. Opt.*, vol. 57, no. 17, p. 4839, Jun. 2018.

[32] A. N. Bashkatov, É. A. Genina, V. I. Kochubey, and V. V. Tuchin, "Optical properties of the subcutaneous adipose tissue in the spectral range 400–2500 nm," *Opt. Spectrosc.*, vol. 99, no. 5, p. 836, 2005.

[33] A.-K. Kirchherr, A. Briel, and K. Mäder, "Stabilization of indocyanine green by encapsulation within micellar systems," *Mol. Pharm.*, vol. 6, no. 2, pp. 480–491, Feb. 2009.

[34] O. Yadid-Pecht and R. Etienne-Cummings, *CMOS Imagers: From Phototransduction to Image Processing*. Springer Science & Business Media, 2007.

[35] Y. Nakamura, A. Mochida, P. L. Choyke, and H. Kobayashi, "Nanodrug delivery: Is the enhanced permeability and retention effect sufficient for curing cancer?" *Bioconjug. Chem.*, vol. 27, no. 10, pp. 2225–2238, Oct. 2016.

[36] LI-COR, "IRDye® 800CW 2-DG optical probe," 2018. [Online]. Available: https://www.licor.com/bio/products/reagents/irdye/2dg/index.html. [Accessed: 20-Nov-2018].

[37] LI-COR, "EGF optical probe overview - Why target EGFR?" 2018. [Online]. Available: https://www.licor.com/bio/products/reagents/irdye/egf/. [Accessed: 20-Nov-2018].

[38] M. Longmire, P. L. Choyke, and H. Kobayashi, "Clearance properties of nano-sized particles and molecules as imaging agents: considerations and caveats," *Nanomedicine (Lond).*, vol. 3, no. 5, pp. 703–17, Oct. 2008.

[39] G. Hong, A. L. Antaris, and H. Dai, "Near-infrared fluorophores for biomedical imaging," *Nat. Biomed. Eng.*, vol. 1, no. 1, Jan. 2017.

[40] Q. T. Nguyen and R. Y. Tsien, "Fluorescence-guided surgery with live molecular navigation — a new cutting edge," *Nat. Rev. Cancer*, vol. 13, no. 9, pp. 653–662, Sep. 2013.

[41] D. X. D. Yang and A. El Gamal, "Comparative analysis of SNR for image sensors with enhanced dynamic range," in *Sensors, Cameras, and Systems for Scientific/Industrial Applications*, 1999, vol. 3649, pp. 197–211.

[42] S. Decker, D. McGrath, K. Brehmer, and C. G. Sodini, "A 256×256 CMOS imaging array with wide dynamic range pixels and column-parallel digital output," *IEEE J. Solid-State Circuits*, vol. 33, no. 12, pp. 2081–2091, 1998.

[43] D. X. D. Yang, A. El Gamal, B. Fowler, and Hui Tian, "A 640×512 CMOS image sensor with ultra wide dynamic range floating-point pixel-level ADC," in *1999 IEEE International Solid-State Circuits Conference (ISSCC). Digest of Technical Papers (Cat. No.99CH36278)*, 1999, pp. 308–309.

[44] S. Kleinfelder, Suki-Iwan Lim, Xinqiao Liu, and A. El Gamal, "A 10 kframe/s 0.18 μm CMOS digital pixel sensor with pixel-level memory," in *2001 IEEE International Solid-State Circuits Conference (ISSCC). Digest of Technical Papers (Cat. No.01CH37177)*, 2001, pp. 88–89.

[45] C. Mead, "Neuromorphic electronic systems," *Proc. IEEE*, vol. 78, no. 10, pp. 1629–1636, 1990.

[46] A. Vanarse, A. Osseiran, and A. Rassau, "A review of current neuromorphic approaches for vision, auditory, and olfactory sensors," *Front. Neurosci.*, vol. 10, Mar. 2016.

[47] C. Posch, T. Serrano-Gotarredona, B. Linares-Barranco, and T. Delbruck, "Retinomorphic event-based vision sensors: Bioinspired cameras with spiking output," *Proc. IEEE*, vol. 102, no. 10, pp. 1470–1484, Aug. 2014.

[48] S. Kavadias, B. Dierickx, D. Scheffer, A. Alaerts, D. Uwaerts, and J. Bogaerts, "A logarithmic response CMOS image sensor with on-chip calibration," *IEEE J. Solid-State Circuits*, vol. 35, no. 8, pp. 1146–1152, Aug. 2000.

[49] W. Yang, "A wide-dynamic-range, low-power photosensor array," in *1994 IEEE International Solid-State Circuits Conference (ISSCC). Digest of Technical Papers*, 1994, pp. 230–231.

[50] P. Lichtsteiner, C. Posch, and T. Delbruck, "A 128 x 128 120dB 30mW asynchronous vision sensor that responds to relative intensity change," in *2006 IEEE International Solid State Circuits Conference (ISSCC). Digest of Technical Papers*, 2006, pp. 2060–2069.

[51] C. Posch, D. Matolin, and R. Wohlgenannt, "A QVGA 143dB dynamic range asynchronous address-event PWM dynamic image sensor with lossless pixel-level video compression," in *2010 IEEE International Solid-State Circuits Conference (ISSCC). Digest of Technical Papers*, 2010, pp. 400–401.

[52] D. Matolin, C. Posch, and R. Wohlgenannt, "True correlated double sampling and comparator design for time-based image sensors," in *2009 IEEE International Symposium on Circuits and Systems*, 2009, pp. 1269–1272.

[53] C. Posch, D. Matolin, and R. Wohlgenannt, "A QVGA 143 dB dynamic range frame-free PWM image sensor with lossless pixel-level video compression and time-domain CDS," *IEEE J. Solid-State Circuits*, vol. 46, no. 1, pp. 259–275, Jan. 2011.

[54] A. D. McNaught and A. Wilkinson, *Compendium of Chemical Terminology*, 2nd ed. Oxford: Blackwell Scientific Publications, 1997.